PHYSICAL REVIEW E **81**, 026306 (2010)

# Coarsening in the electrohydrodynamic patterning of thin polymer films

Ning Wu,[*] Michail E. Kavousanakis, and William B. Russel[†]
*Department of Chemical Engineering, Princeton University, Princeton, New Jersey 08544-5263, USA*

(Received 24 August 2009; published 12 February 2010)

Periodic pillarlike microstructures can be created from initially flat polymer films via the electrohydrodynamic instabilities. Those patterns, however, are metastable. Our experimental observations show that the average pillar size increases slowly after linear growth. Major coarsening events then take place over times several orders of magnitude longer than the linear growth time. For all fill ratios, a logarithmic time dependence of the average pillar size can be identified, i.e., $\langle S \rangle \propto \ln t$. Thicker films, however, have faster coarsening rates than thinner films. Linear stability analysis of the pseudosteady states reveals two major coarsening mechanisms, collision and Ostwald ripening, which can also be identified from experimental images. We then reduce the original partial differential equation (PDE) into a pair of ODEs, which govern the interaction between pillars due to the above two coarsening mechanisms. From this, a logarithm scaling law is obtained for both low and high fill ratios and the coarsening rate is slower for lower fill ratios, consistent with experimental observations. We also find that arrays with more uniform sizes tend to start coarsening later, but they coarsen faster than more "disperse" arrays, which could be possibly utilized in experiments for controlling the onset and speed of coarsening. The logarithm scaling in the electrohydrodynamic coarsening phenomenon, which differs from coarsening in spinodal decomposition and dewetting of thin liquid films, is due to the significant nonlinear effect of Maxwell stresses and geometric confinement on the disjoining pressure at both top and bottom electrodes.

DOI: 10.1103/PhysRevE.81.026306 PACS number(s): 47.20.Ma, 47.54.Jk, 47.65.−d

## I. INTRODUCTION

Creating micropatterns and nanopatterns of polymeric materials on surfaces is of great interest in microdevice fabrication and materials engineering. In addition to photolithographic and soft lithographic techniques [1], a nonlithographic method called the "electrohydrodynamic (EHD) patterning" of thin polymeric films [2,3] has demonstrated promising potential due to its low cost and versatility in making three-dimensional patterns even without a prepatterned mask. Shown schematically in Fig. 1, the originally flat and molten interface of polymer-air or polymer-polymer bilayer fluids is destabilized by a normal electric field generated either externally or internally. The destabilization is due to the Maxwell stress that arises at the bilayer interface when the dielectric constants mismatch. Large scale periodic arrays of pillars (with diameters on the order of microns) can be easily created out of thin polymer films even under a piece of unpatterned mask. Competition between the Maxwell stress and capillary pressure selects a characteristic spacing between pillars, which depends on various process parameters [4]. Features as small as 100 nm can also be replicated faithfully with a patterned mask [3]. Those periodic structures, however, are metastable. Our primitive numerical studies [5] have indicated that those pillars continue to evolve, via a cascade of merging processes among neighboring pillars, toward its thermodynamically stable state, which is one single pillar with an infinitely large period or a period equal to the computational domain $L$. On one hand, such coarsening can deteriorate the quality of the original periodic patterns unintentionally. On the other hand, it can be utilized purposely to change the morphology of initial patterns and create novel patterns that are distinctive from those patterns on the mask, as demonstrated in one of our recent studies [6]. Therefore, we are motivated to study the coarsening dynamics in EHD patterning via both experiments and a variety of theoretical and numerical tools. Better understanding of this coarsening phenomenon is desired if one wishes to control the patterns that are formed in this highly dynamic process.

Although coarsening during phase separation in liquid mixtures has been studied extensively via experiments, theories, and numerical simulations [7,8], it is also observed in other situations, such as Marangoni convection in liquid films [9,10] and dewetting of thin films [11–13]. These new coarsening phenomena resemble spinodal decomposition in morphology and mathematical formulation, but each physi-

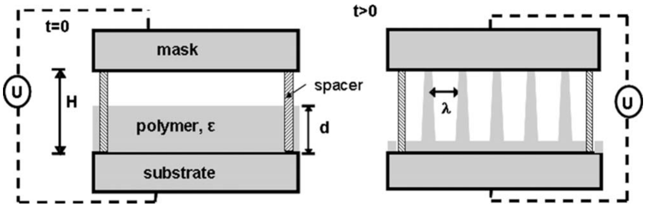

FIG. 1. The schematics of the experimental setup to study long-time dynamics of the electrohydrodynamic patterning of thin polymer films. Due to a mismatch of the dielectric constants (ε) between air and polymer, the originally flat polymer-air interface can be destabilized by a normal electric field applied between mask and substrate. Arrays of pillars with a constant spacing can be generated if the polymer is melted.

---

[*] Present address: School of Enginppeering and Applied Science, Harvard University, Cambridge.

[†] Author to whom correspondence should be addressed; wbrussel@princeton.edu

1539-3755/2010/81(2)/026306(13)

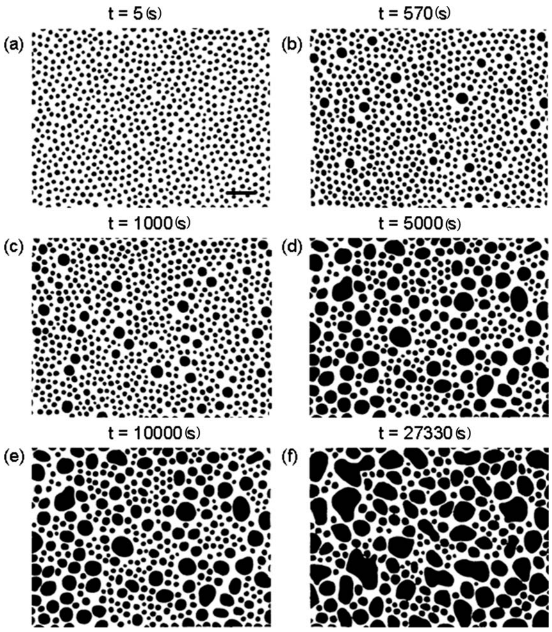

FIG. 2. Optical images illustrating different stages for the coarsening of 160-nm-PDMS (600*k* cSt) film under a constant voltage of 17 V. The fill ratio, defined by the ratio of initial film thickness to mask-substrate separation $h_0 = d/H$, is equal to 0.6. The scale bar in (a) represents 10 $\mu$m.

cal system has its own unique characteristics and there is no universal scaling law for coarsening. We hope to uncover the unique characteristics in this system and illuminate the factors reflected in the scaling law. Our theoretical formulation in one dimension provides qualitative agreement with two-dimensional (2D) experimental results and reveals intriguing uniqueness in the coarsening induced by EHD instabilities.

This paper is organized as follows. In the following section, we describe experimental explorations on the coarsening phenomenon. In Sec. III, we introduce our theory with a brief description on the formulation of the problem and the derivation of thermodynamically stable and pseudo-steady-states film profiles. Mechanisms for coarsening will be discussed in Sec. IV on the basis of perturbation studies of those pseudosteady states. In Sec. V, we will perform numerical simulations incorporating the coarsening modes justified. The scaling law for coarsening can then be extracted. Experimental observations will be compared with numerical results. Finally, the conclusions are summarized in Sec. VI.

## II. COARSENING: EXPERIMENTAL EXPLORATIONS

To understand the long-time dynamics of the pattern formation induced by the EHD instability, we designed and performed real time observations with an optical microscope. A series of polydimethylsiloxane (PDMS) films with thicknesses ranging from 50 to 300 nm were prepared on $\mathrm{SiO}_x/\mathrm{Si}$ substrates by spin coating. The reasons for selecting PDMS as our model polymer were twofold. First, its glass transition temperature $T_g$ is well below room temperature, so heating, which is not desirable on the stage of a microscope, can be avoided. Second, PDMSs with a broad range of viscosities (1–20 000 000 cSt) are commercially available, allowing the time scale of polymer flow (and coarsening), which depends on viscosity, to be varied over a broad range. Cyclohexane proved to be a good solvent for spin coating uniform films of PDMS. A glass slide coated with ~150 nm ITO was used as the mask to preserve transparency. Real time images taken by the Olympus MX40 optical microscope with different time intervals were then converted to black and white pixels and analyzed with a free software IMAGEJ [14]. Several important parameters are the initial film thickness $d$, mask-substrate separation $H$, interfacial tension $\gamma$, polymer viscosity $\mu$, dielectric constant of polymer $\varepsilon$, and the externally applied voltage $U$.

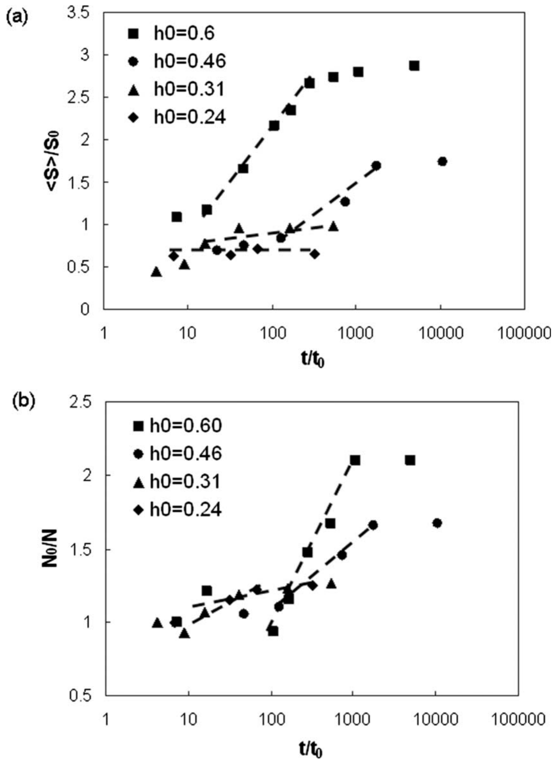

FIG. 3. Coarsening data for PDMS films (100*k* cSt) with different fill ratios. Logarithm dependence on time can be identified and at later stage, coarsening becomes even slower.

Figure 2 records the time evolution of a 160-nm-thin PDMS film under a constant voltage of 17 V for 8 h. The fill ratio defined by the ratio of initial film thickness to the mask-substrate separation, $h_0 = d/H$, is 0.6. Black regions in the binary images represent polymer pillars and the white corresponds to the substrate. Coarsening is evident, as can be identified visually as an increase in average size per pillar and a decrease in the number of pillars over time. We quantify the coarsening dynamics by plotting the average projected contact area per pillar $\langle S \rangle$ as function of time for different fill ratios in Fig. 3. The area $\langle S \rangle$ is normalized by $S_0 \sim \sqrt{3} h_0 \lambda_{\max}^2 / 2$, which is the area of one cylindrical pillar in a perfect hexagonal array, whose spacing $\lambda_{\max}$ is set by the prediction from the linear instability theory [4]. Similarly, the time $t$ is scaled by $t_0$, the time estimated to grow full pillars based on the same theory. For intermediate and high fill ratios, the normalized pillar size increases slowly after linear growth, due to accidental coarsening among very close pillars. The major part of coarsening, however, takes place over times several orders of magnitude longer than the linear growth time. Straight lines in the linear-logarithm plot indicate the logarithmic dependence on time, i.e., $\langle S \rangle \propto \ln t$ with faster rate for larger fill ratios (or equivalently, thicker films), which is consistent with previous reports [15]. At much later stages, the coarsening rate becomes even slower. For the lowest fill ratio $h_0 = 0.24$, the average pillar size hardly changes within the experimental time. Similar trends were observed in the evolution of the number of pillars too.

## III. FORMULATION OF THE PROBLEM AND STEADY-STATE SOLUTIONS

The partial differentail equation (PDE) that describes the height evolution of thin liquid film under a normal electric field in one dimension can be written in the form as [4,5,16]

$$\frac{\partial h}{\partial t} = \frac{\partial}{\partial x}\left(h^3 \frac{\partial P}{\partial x}\right), \qquad (1)$$

where pressure $P$ consists of capillary pressure, Maxwell stress, and disjoining pressure, $P = -\partial^2 h/\partial x^2 + g(h)$. For convenience, the Maxwell stress and disjoining pressure are expressed in dimensionless form

$$g(h) = \frac{df}{dh} = -\frac{(\varepsilon - 1)\varepsilon}{2[h + (1-h)\varepsilon]^2} + \frac{A}{(1-h)^3} - \frac{A}{h^3},$$

$$f(h) = -\frac{\varepsilon}{2[h + \varepsilon(1-h)]} + \frac{A}{2h^2} + \frac{A}{2(1-h)^2}. \qquad (2)$$

We define a length scale $L = (\gamma H^3/\varepsilon_0 U^2)^{1/2}$ (where $\varepsilon_0$ is the permittivity of vacuum) and a time scale $\tau = 3H^3 \mu \gamma / (\varepsilon_0 U^2)^2$ so that the coordinate and time can be nondimensionalized through $x \rightarrow x/L$ and $t \rightarrow t/\tau$. In addition, the film thickness, pressure, dielectric contrast, and Hamaker constant are also in their dimensionless form, i.e., $h \rightarrow h/H$, $P \rightarrow PH^2/U^2\varepsilon_0$, $\varepsilon = \varepsilon_{bottom}/\varepsilon_{top}$, and $A \rightarrow A/HU^2\varepsilon_0$. Unless mentioned specifically, from now on all variables are referred in their dimensionless forms.

A trivial solution of Eq. (1) is $h = h_0$. However, it is linearly unstable to small amplitude disturbances, as demonstrated in the previous analyses [4,16]. Based on the dispersion relation, a fastest growing wave with wavelength $\lambda = \lambda_{\max}$ is predicted in good agreement with the pillar-to-pillar spacing observed in experiments. By following the dynamics of Eq. (1) into nonlinear regimes, we have found that the system lingers around several other pseudosteady states with increasing wavelength $\lambda$ and decreasing $|P - P_0|$ until reaching the thermodynamically stable state, in which $P = P_0$ and $\lambda \rightarrow \infty$ [5]. Therefore, the coarsening phenomenon is closely related to the stability of the pseudosteady states. In this section, we will obtain those states through a perturbative analysis similar to Refs. [17,18]. In Secs. IV and V, the stability of those pseudosteady states will be assessed. Based on which, we can identify different coarsening modes and compare them with our experimental observations. A logarithmic scaling law can then be deduced from simulations based on those coarsening modes in good qualitative agreement with experimental results.

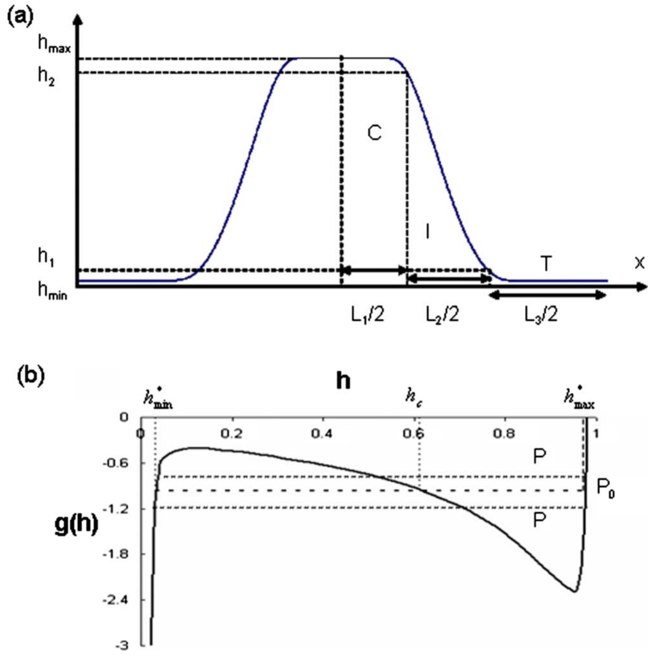

FIG. 4. (a) (Color online) A schematic of the steady-state profile of the film in one dimension, which has a period of $\lambda = L_1 + L_2 + L_3$. The profile is divided into three regimes: Core, Intermediate, and Tail. The steady state is characterized by the equilibrium pressure $P$, maximal thickness $h_{\max}$, minimal thickness $h_{\min}$, and period $\lambda$. At $h = h_{\max}$ and $h = h_{\min}$, $d^2h/dx^2$ vanishes in the thermodynamically stable state, while it is nonzero for pseudosteady states. (b) The Maxwell construction in the plot of $g(h)$ vs $h$ determines both $h^*_{\min}$ and $h^*_{\max}$. $h_c$ corresponds to the Maxwell point. The pseudo-steady-state pressure $P$ approaches from the top (or bottom) to the thermodynamically stable state pressure $P_0$ if the initial film thickness $h_0$ is smaller (or larger) than $h_c$.

To find the steady state, we set the time derivative, $\partial h/\partial t$ in Eq. (1), equal to zero, yielding a constant flux $h^3 \partial P/\partial x$. For a stationary steady state, this flux is zero and pressure is a constant. In other words, the steady-state solutions correspond to the pillar profile, in which pressure is spatially uniform,

$$g(h) - d^2h/dx^2 = P. \qquad (3)$$

There are many solutions to the above equation since $g(h)$ is highly nonlinear. A typical steady-state pillar profile is shown in Fig. 4(a). We categorize them into two types: the thermodynamically stable state and pseudosteady states. Imagine that the originally flat interface $h_0$, a homogenous state, evolves under the influence of the electric field into periodic structures in which $h_{\max}$ and $h_{\min}$ deviate from $h_0$. The first important pseudosteady state that a system reaches has a period conformable to the prediction of the linear stability theory, i.e., $\lambda = \lambda_{\max}$. The profile then lingers around several other pseudosteady states, evolving from less stable to more stable states, characterized by a set of parameters $\{P, h_{\max}, h_{\min}, \lambda\}$, which depends on the initial film thickness. The destination of such coarsening is the thermodynamically stable state in which $P=P_0$, $\lambda \rightarrow \infty$, $h_{\max}=h^*_{\max}$, and $h_{\min}=h^*_{\min}$, independent of the initial film thickness. During the coarsening process, the difference between the pseudosteady state and thermodynamically stable state, characterized by $P-P_0$, $h_{\max}-h^*_{\max}$, and $h_{\min}-h^*_{\min}$, becomes vanishingly small. Although $h_{\max}$ is always smaller than $h^*_{\max}$ and $h_{\min}$ is always larger than $h^*_{\min}$, $P-P_0$ can be either positive or negative, depending on whether the initial film thickness $h_0$ is thinner than Maxwell point $h_c$ or not. We will find solutions of Eq. (3) for the thermodynamically stable and pseudosteady states in Secs. III A and III B, respectively.

### A. Thermodynamically stable state

The thermodynamically stable state has been discussed in Ref. [5], but for sake of completeness, we summarize it briefly here. In addition, we present an asymptotic estimate of the thermodynamically stable state, which matches numerical calculations very well. Integrating Eq. (3) over $h$ and evaluating the integral at both $h_{\max}$ and $h_{\min}$ gives

$$f(h_{\max}) - f(h_{\min}) - P(h_{\max} - h_{\min}) = 0. \tag{4}$$

At the thermodynamically stable state, the curvature term $d^2h/dx^2$ in Eq. (3) vanishes at $h_{\max}$ and $h_{\min}$. Therefore, Eqs. (3) and (4) can be simplified as

$$g(h^*_{\max}) = P_0,$$

$$g(h^*_{\min}) = P_0,$$

$$f(h^*_{\max}) - f(h^*_{\min}) - P_0(h^*_{\max} - h^*_{\min}) = 0. \tag{5}$$

Equations (5) consist of three algebraic equations that can be solved numerically to obtain $h^*_{\max}$, $h^*_{\min}$, and $P_0$. Equivalently, they can be found graphically via a Maxwell construction in the plot of $g(h)$ vs $h$, as shown in Fig. 4(b). In general, the van der Waals interaction is short ranged compared with the electrostatic force and therefore has little effect on the period $\lambda_{\max}$. The Hamaker constant, however, has important influences on $h^*_{\max}$ and $h^*_{\min}$, which are mainly determined by the balance of the electrostatic and disjoining pressure near the top and bottom electrodes. A larger (smaller) Hamaker constant at the top (bottom) would result in a smaller value of $h^*_{\max}$ ($h^*_{\min}$).

Equations (5) and the graphical construction remind us what we know about the macrophase separation in classical thermodynamics, suggesting a convenient analog. In fact, Eq. (1) is a generalized Cahn-Hilliard-type equation [19] with $h^3$ playing the role of the mobility. Correspondingly, we can define a Lyapunov functional $F$

$$F = \int \left[ f(h) + \frac{1}{2}(dh/dx)^2 \right] dx \tag{6}$$

and transform Eq. (1) into

$$\frac{dF}{dt} = - \int h^3 \left[ \nabla \frac{\delta F}{\delta h} \right]^2 dx. \tag{7}$$

Clearly, $F$ is a monotonically decreasing function of time that we have proved to correspond to the energy of the system [5]. Here $f(h)$ represents the (macroscopic) Helmholtz free-energy density of a film with uniform thickness $h$. The initial film $h_0$ is absolutely unstable between two extrema in $g(h)$(the spinodals), while it is bistable between $h^*_{\max}$ and $h^*_{\min}$ (the binodals). Any initial state within the spinodal tends to "separate" into "two phases:" a thicker film and a thinner film in order to minimize its free-energy density $f(h)$. The term $(dh/dx)^2$ in the Lyapunov functional $F$ characterizes the energy density associated with interfacial curvature, which provides another driving force for coarsening. To minimize this interfacial "penalty," the structures continue evolving until they have the largest possible period, i.e., the infinity. Such a structure has the minimum number (one only) of sharp transitions between the two equilibrium thicknesses. Thus, it is preferred for thermodynamic reasons.

In the following, we derive the asymptotic solutions of the thermodynamically stable state, i.e., the equilibrium thicknesses $h^*_{\max}$ and $h^*_{\min}$, pressure $P_0$, and inflection point $h_c$. Since $h^*_{\max} \sim 1$ and $h^*_{\min} \sim 0$, we can expand as

$$h^*_{\min} = 0 + \delta h^1_{\min} + O(\delta^2),$$

$$h^*_{\max} = 1 + \delta h^1_{\max} + O(\delta^2), \tag{8}$$

where $\delta$ is a small parameter and let $\delta = A^{1/3}$ for algebraic simplicity. Similarly, pressure $P_0$ and $h_c$ can also be expressed as

$$P_0 = P^0 + \delta P^1 + O(\delta^2),$$

$$h_c = h^0_c + \delta h^1_c + O(\delta^2). \tag{9}$$

Substituting Eqs. (8) and (9) into Eqs. (5) and collecting terms with the same order of $\delta$, we can have at zero order,

$$P^0 = -\frac{\varepsilon - 1}{2}, \quad h^0_c = \frac{\varepsilon - \sqrt{\varepsilon}}{\varepsilon - 1}. \tag{10}$$

At first order,

$$h^1_{\min} = \left[ \frac{2\varepsilon}{(\varepsilon - 1)^2} \right]^{1/3}, \quad h^1_{\max} = -\left[ \frac{2}{(\varepsilon - 1)^2} \right]^{1/3},$$

$$P^1 = \frac{3}{2}\left[ \frac{1}{(h^1_{\max})^2} - \frac{1}{(h^1_{\min})^2} \right], \quad h^1_c = -\frac{P^1[h^0_c + \varepsilon(1 - h^0_c)^2]^3}{\varepsilon(\varepsilon - 1)^2}. \tag{11}$$

Figure 5 shows that the first-order approximations agree very well with the numerical solutions of Eqs. (5). The polymer film approaches both mask and substrate ($h^*_{\max} \rightarrow 1$ and $h^*_{\min} \rightarrow 0$) when $\varepsilon$ moves away from unity. The equilibrium pressure $P_0$ is positive when (the dielectric contrast) $\varepsilon < 1$ and negative when $\varepsilon > 1$, through a monotonic function of $\varepsilon$.

### B. Pseudosteady states

In addition to the thermodynamically stable states derived above, there exist a large number of other solutions that satisfy Eq. (3). We call them pseudosteady states because they are linearly unstable to small perturbations, as we will show

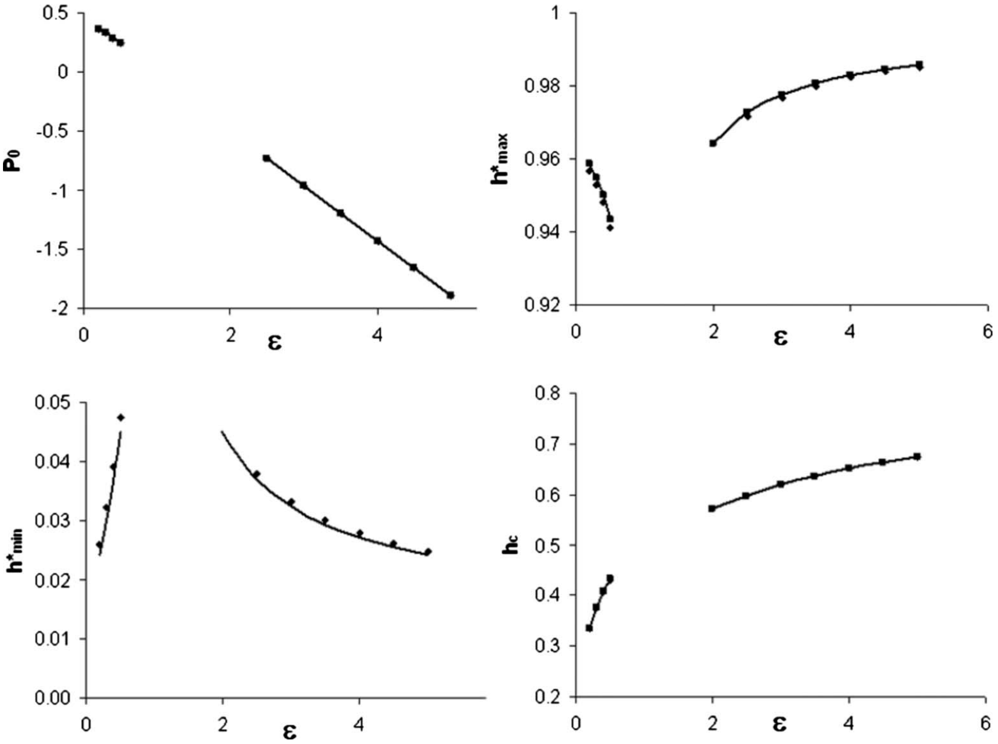

FIG. 5. Comparison between the asymptotic approximation (lines) and numerical solution (dots) of the thermodynamically stable steady state characterized by $h^*_{\max}$, $h^*_{\min}$, $P_0$, and $h_c$. The effective Hamaker constant $A$ is kept constant.

in the next section. Since the instabilities of those pseudosteady states will determine the rate of coarsening, it is important to identify and characterize them. A pseudosteady state is represented schematically in Fig. 4(a). Both the top and bottom of the pillar have almost flat regions because of very small curvatures at those extrema. We therefore divide the pseudo-steady-state profile into three regimes: the Core, Intermediate, and Tail with widths $L_1$, $L_2$, and $L_3$, respectively. The corresponding thicknesses $h_1$ and $h_2$, which are close to $h_{\max}$ and $h_{\min}$, can be chosen arbitrarily. For the sake of convenience, we let $h_1=1.01h_{\min}$ and $h_2=0.99h_{\max}$.

To obtain the profile of a pseudosteady state, one can integrate Eq. (3) over $h$ and evaluate the integral at $h_{\max}$ and $h$,

$$\frac{1}{2}\left(\frac{dh}{dx}\right)^2=[f(h)-Ph]-[f(h_{\max})-Ph_{\max}]=V(h)-V_0. \tag{12}$$

Clearly, given the equilibrium pressure $P$ and the maximal thickness $h_{\max}$, one can further integrate Eq. (12) numerically to obtain the solution, from which the period $\lambda$ and initial fill ratio $h_0$ can then be calculated. Nonetheless, integration of Eq. (12) in the vicinity of $h_{\max}$ and $h_{\min}$ is challenging numerically because $dh/dx$ vanishes at those extrema. In the following, we attempt to utilize asymptotic expansions to obtain the solutions of pseudosteady states semianalytically.

Since $h_{\max}$ and $h_{\min}$ are close to $h^*_{\max}$ and $h^*_{\min}$, we linearize $f(h_{\max})$ and $f(h_{\min})$ around $h^*_{\max}$ and $h^*_{\min}$ in Eq. (4). After some algebraic simplifications, we have

$$\begin{aligned}\frac{g'(h^*_{\max})}{2}(h^*_{\max}-h_{\max})^2-\frac{g'(h^*_{\min})}{2}(h_{\min}-h^*_{\min})^2 \\ +O[(h^*_{\max}-h_{\max})^3]+O[(h_{\min}-h^*_{\min})^3] \\ =(P-P_0)[(h^*_{\max}-h^*_{\min})-(h^*_{\max}-h_{\max}) \\ -(h_{\min}-h^*_{\min})].\end{aligned} \tag{13}$$

The leading-order term on the right-hand side is $(P-P_0)(h^*_{\max}-h^*_{\min})\sim O(P-P_0)$. Therefore, a natural expansion on $h^*_{\max}-h_{\max}$ and $h_{\min}-h^*_{\min}$ in terms of $P-P_0$ would be

$$\begin{aligned}h^*_{\max}-h_{\max}&=a_1|P-P_0|^{1/2}+a_2|P-P_0|+O(|P-P_0|^{3/2}),\\ h_{\min}-h^*_{\min}&=b_1|P-P_0|^{1/2}+b_2|P-P_0|+O(|P-P_0|^{3/2}).\end{aligned} \tag{14}$$

We also linearize $g(h)$ in Eq. (3) around $h_{\max}$,

$$\frac{d^2h}{dx^2}=g'(h^*_{\max})h+P_0-P-g'(h^*_{\max})h^*_{\max}+O[(h^*_{\max}-h_{\max})^2]. \tag{15}$$

Given that $h(0)=h_{\max}$ and $h'(0)=0$, we can obtain the profile in the core regime,

$$\begin{aligned}h_{\max}-h\approx[h^*_{\max}-h_{\max}-(P_0-P)/g'(h^*_{\max})]\\ \times\{\cosh[x\sqrt{g'(h^*_{\max})}]-1\}.\end{aligned} \tag{16}$$

Similarly, the profile in the tail regime is

$$h - h_{\min} \approx [h_{\min} - h^*_{\min} - (P - P_0)/g'(h^*_{\min})] \times \{\cosh[x\sqrt{g'(h^*_{\min})}] - 1\}. \tag{17}$$

Notice that $g'(h^*_{\max})$ and $g'(h^*_{\min})$ are of the same order of magnitude, e.g., $g'(h^*_{\max}) \sim 129$ and $g'(h^*_{\min}) \sim 44$ for $\varepsilon = 2.5$ and $A = 0.000\,01$. Combining Eqs. (13), (16), and (17) with the asymptotic expansion [Eqs. (14)] will yield the pseudosteady-state profiles. Depending on the relative magnitude of $h^*_{\max} - h_{\max}$ and $h_{\min} - h^*_{\min}$, we can divide the pseudosteady states into three categories.

### 1. High fill ratio limit

If $(h_{\min} - h^*_{\min}) \gg (h^*_{\max} - h_{\max})$, substituting Eqs. (14) with $a_1 = 0$ and $b_1 \neq 0$ into Eq. (13), to the leading order yields

$$h_{\min} - h^*_{\min} = b_1 (P_0 - P)^{1/2} + O[(P_0 - P)], \tag{18}$$

where $b_1 = \sqrt{2(h^*_{\max} - h^*_{\min})/g'(h^*_{\min})}$.

Substituting Eq. (18) in Eq. (17), we obtain

$$h - h_{\min} \approx b_1 (P_0 - P)^{1/2} \{\cosh[x\sqrt{g'(h^*_{\min})}] - 1\}. \tag{19}$$

Therefore, given a pressure $P$ or $(P_0 - P)$, one can obtain $h_{\min}$ and the profile in the tail regime according to Eqs. (18) and (19). The width of the tail $L_3$ is then determined by the position of $x$, where $h = h_1 = 1.01 h_{\min}$,

$$\cosh[L_3\sqrt{g'(h^*_{\min})}/2] = 1 + \frac{0.01 h_{\min}}{b_1 (P_0 - P)^{1/2}}. \tag{20}$$

Similarly, substituting $h^*_{\max} - h_{\max} = a_2 (P_0 - P) + O(P_0 - P)^{3/2}$ into Eq. (16) yields the profile in the core regime

$$h_{\max} - h \approx (P_0 - P)[a_2 - 1/g'(h^*_{\max})]\{\cosh[x\sqrt{g'(h^*_{\max})}] - 1\}. \tag{21}$$

The width of the core $L_1$ is determined by the position of $x$, where $h = h_2 = 0.99 h_{\max}$,

$$\cosh[L_1\sqrt{g'(h^*_{\max})}/2] = 1 + \frac{0.01 h_{\max}}{[a_2 - 1/g'(h^*_{\max})](P_0 - P)}. \tag{22}$$

With the heights in the core and tail regimes calculated, the profile in the intermediate regime can be obtained via numerical integration of Eq. (3) with the initial conditions of $h(0) = h_2 = 0.99 h_{\max}$ and $h'(0) = -\sqrt{2[V(h_2) - V_0]}$. The width of the intermediate part $L_2$ is simply the length over which $h$ changes from $h_2$ to $h_1$, and the mass $M_2$ is obtained by integrating the height profile over $x$.

Therefore, the assumption of $(h_{\min} - h^*_{\min}) \gg (h^*_{\max} - h_{\max})$ provides a simple route to determine the pseudo-steady-state profile for a given pressure $P$ and fill ratio $h_0$: Eqs. (18) and (19) define the profile in tail regime, the core regime is obtained from Eq. (21), and finally solving Eq. (3) numerically yields the intermediate regime. Once the pseudo-steady-state profile is obtained, simple relations yield the period and fill ratio too,

$$\lambda = L_1 + L_2 + L_3,$$

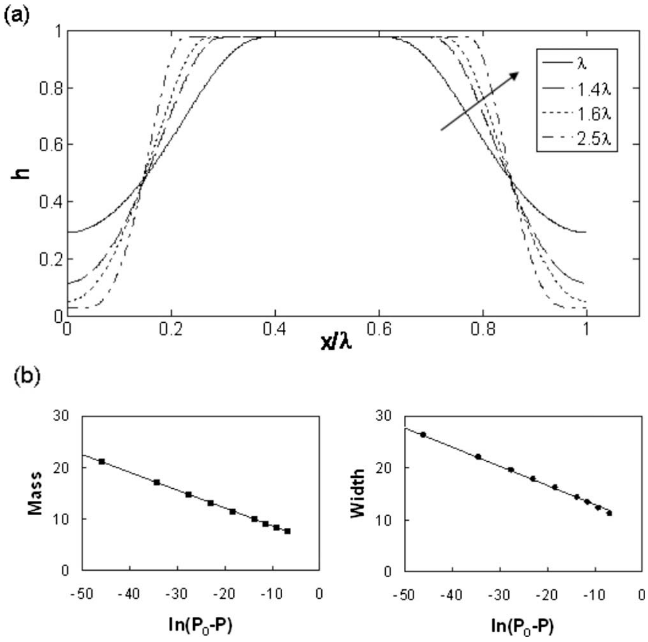

FIG. 6. (a) The pseudo-steady-state profile for $h_0 = 0.7$ with different periods (hence, different pressure $P_0 - P$). The smallest period is $\lambda_{\max}$, the most unstable wavelength in linear stability analysis. Following the arrow's direction, $P_0 - P$ decreases and $\lambda$ increases. (b) The mass $M$ and width $W$ of the pillar (core + intermediate regimes) are linear functions of $Q = \ln(P_0 - P)$.

$$h_0 = (L_1 h_{\max} + M_2 + L_3 h_{\min})/(L_1 + L_2 + L_3). \tag{23}$$

The coefficient $a_2$ in Eq. (21) is chosen to satisfy Eqs. (23) for a given fill ratio $h_0$ via several iterations.

Figure 6(a) shows a series of pseudo-steady-state profiles for a constant fill ratio of $h_0 = 0.7$ with different periods (hence different pressure $P$). The $x$ axis has been scaled with its period for each curve. Following the arrow's direction, $P_0 - P$, $h^*_{\max} - h_{\max}$, and $h_{\min} - h^*_{\min}$ decrease and $\lambda$ increases. It should be noted that when $\lambda < 1.6\lambda_{\max}$, $h_{\min}$ is much greater than $h^*_{\min}$, i.e., the curvature at $h_{\min}$ is relatively large. This makes the asymptotic expansion of $h_{\min} - h^*_{\min}$ on $P_0 - P$ inaccurate. Therefore, we obtained those steady-state profiles by integrating Eq. (12) directly with $L_3 = 0$, i.e., essentially no tail regime exists. When $\lambda$ is longer than $1.6\lambda_{\max}$, both $h^*_{\max} - h_{\max}$ and $h_{\min} - h^*_{\min}$ become vanishingly small with increasing period but follow different orders of $P_0 - P$. One of the key features in Fig. 6(a) is that for high fill ratios, the residual layer thickness $h_{\min}$ can be relatively thick (i.e., $h_{\min} \gg h^*_{\min}$) when the period is not too far from $\lambda_{\max}$. Since the flux depends strongly on film thickness ($J \propto h^3$), merging of neighboring pillars can be relatively fast for high fill ratio films, especially when the periods are close to $\lambda_{\max}$. The mass within the core and intermediate regimes, i.e., $M = L_1 h_{\max} + M_2$ is a linear function of $Q = \ln(P_0 - P)$, as shown in Fig. 6(b). The same relationship also applies for the width of the pillar, defined as $W = L_1 + L_2$. Therefore, $Q$, instead of $P$, is a more appropriate process variable. In the following, we will simply refer $Q$ as the (reduced) "pressure."

Before closing the discussion of the "high fill ratio limit," let us ponder the physical meaning of our key assumption in this part, i.e., $h_{\min}-h^*_{\min}\sim O[(P_0-P)^{1/2}]$ and $h^*_{\max}-h_{\max}\sim O[(P_0-P)]$. Their dependence on different orders of pressure $P_0-P$ indicates that the width of the core $L_1$ is generally much greater than the width of the tail $L_3$ or equivalently, the core is much "flatter" than the tail, as is mathematically evident by direct comparison of Eqs. (20) and (22) and demonstrated clearly in Fig. 6(a). When $\lambda < 1.6\lambda_{\max}$, the tail does not exist at all, and the width of the tail is much narrower than the core even when $\lambda = 2.5\lambda_{\max}$. Since the relative sizes between core and tail also reflect on the fill ratio of the system, it justifies our coinage of the high fill ratio limit.

### *2. Low fill ratio limit*

If $(h^*_{\max}-h_{\max}) \gg (h_{\min}-h^*_{\min})$, substituting Eqs. (14) with $a_1\neq 0$ and $b_1=0$ into Eq. (13), to the leading order, results in

$$h^*_{\max}-h_{\max}=a_1(P-P_0)^{1/2}+O[(P-P_0)],$$

$$h_{\min}-h^*_{\min}=b_2(P-P_0)+O[(P-P_0)^{3/2}], \tag{24}$$

where $a_1=\sqrt{2(h^*_{\max}-h^*_{\min})/g'(h^*_{\max})}$ and $b_2$ must be determined numerically, as discussed later. Substituting Eqs. (24) in Eqs. (16) and (17), we obtain the profiles in the core and tail regimes

$$h_{\max}-h \approx a_1(P-P_0)^{1/2}\{\cosh[x\sqrt{g'(h^*_{\max})}]-1\},$$

$$h-h_{\min}\approx[b_2-1/g'(h^*_{\min})](P-P_0)\{\cosh[x\sqrt{g'(h^*_{\min})}]-1\}. \tag{25}$$

Correspondingly, the widths of the core and tail are

$$\cosh[L_1\sqrt{g'(h^*_{\max})}/2]=1+\frac{0.01h_{\max}}{a_1(P-P_0)^{1/2}},$$

$$\cosh[L_3\sqrt{g'(h^*_{\min})}/2]=1+\frac{0.01h_{\min}}{[b_2-1/g'(h^*_{\min})](P-P_0)}. \tag{26}$$

The intermediate regime can then be obtained via numerical integration of Eqs. (3) with the initial conditions of $h(0)=h_2=0.99h_{\max}$ and $h'(0)=-\sqrt{2[V(h_2)-V_0]}$, and the period and fill ratio of the pseudosteady state are calculated according to Eqs. (23). The coefficient $b_2$ in Eqs. (24) is found by iteration from Eqs. (23) for a given fill ratio $h_0$.

Figure 7(a) depicts a series of the pseudo-steady-state profiles for the same fill ratio $h_0=0.3$ with different periods. Following the arrow direction, $P-P_0$ decreases and $\lambda$ increases. Although not distinguishable in the figure, both $h^*_{\max}-h_{\max}$ and $h_{\min}-h^*_{\min}$ decrease and follow different orders of $P-P_0$, as indicated in Eqs. (24). Pillars of different mass and size have different pressures (and periods), providing the driving force for coarsening. Similar to the high fill ratios, both mass and width depend linearly on $Q=\ln(P-P_0)$.

Equations (26) indicate that the tail is wider than the core, i.e., $L_3 \gg L_1$, so the assumption that $(h^*_{\max}-h_{\max})\gg(h_{\min}-h^*_{\min})$ is more appropriate for low fill ratios. This "low fill ratio limit" has also been assumed implicitly in analyses of coarsening in dewetting of thin films [12,18,20], in which the initial film thickness is usually much smaller than the maximal height of steady-state droplets and droplets are distributed sparsely.

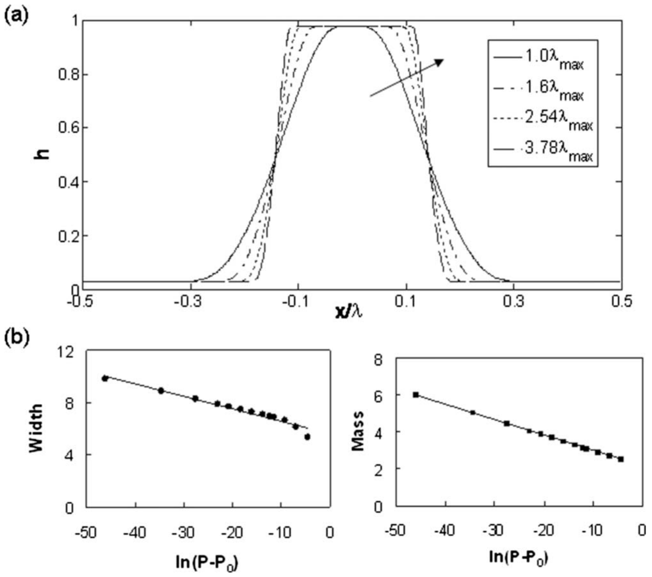

FIG. 7. (a) The steady-state profiles for $h_0=0.3$ with different periods. The smallest period is $\lambda_{\max}=10.99$, the most unstable wavelength. Following the arrow's direction, $P-P_0$ decreases and $\lambda$ increases. (b) The mass and width of the pillar (core and intermediate regimes) are linear functions of $Q=\ln(P-P_0)$.

### *3. Intermediate fill ratio limit*

If $(h^*_{\max}-h_{\max})\sim(h_{\min}-h^*_{\min})$, i.e., $h^*_{\max}-h_{\max}=a_1|P-P_0|^{1/2}$ and $h_{\min}-h^*_{\min}=b_1|P-P_0|^{1/2}$; unfortunately, we are unable to determine the coefficients $a_1$ or $b_1$ *a priori*. Instead, we have

$$a_1^2g'(h^*_{\max})-b_1^2g'(h^*_{\min})=2(h^*_{\max}-h^*_{\min}) \quad \text{if} \quad h_0<h_c,$$

$$a_1^2g'(h^*_{\max})-b_1^2g'(h^*_{\min})=-2(h^*_{\max}-h^*_{\min}) \quad \text{if} \quad h_0>h_c. \tag{27}$$

To determine the pseudo-steady-state profile for a given $P$ and $h_0$, we first guess a value of $a_1$ (or equivalently $h^*_{\max}-h_{\max}$), and then calculate $b_1$ (or $h_{\min}-h^*_{\min}$) from Eqs. (27). Once $h_{\max}$ and $h_{\min}$ is known, the core, tail, and intermediate regimes of the pseudosteady state can be calculated. On one hand, the core's width $L_1$ satisfies

$$\cosh[L_1\sqrt{g'(h^*_{\max})}]=1+\frac{0.01h_{\max}}{a_1(P-P_0)^{1/2}}, \tag{28}$$

on the other hand, Eqs. (23) provides

$$L_1=\frac{L_2h_0-M_2+L_3(h_0-h_{\min})}{h_{\max}-h_0}. \tag{29}$$

A search for the value of $a_1$ that gives the same core width $L_1$ from Eqs. (28) and (29) converges within a few iterations.

Clearly, if we take the limit $a_1\to 0$ (or $b_1\to 0$) in Eqs. (27), we recover the high fill ratio limit (or the low fill ratio

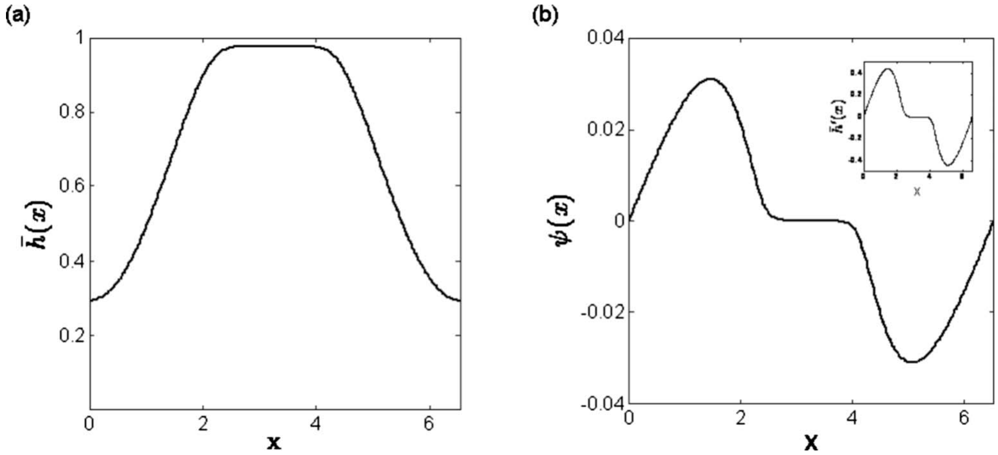

FIG. 8. (a) The steady-state profile $\bar{h}(x)$ with period $\lambda_{\max}$ in a domain of the same size. The initial film thickness is $h_0=0.7$. (b) The eigenfunction that corresponds to the only positive eigenvalue $\omega_1=4.19\times10^{-4}$, which is a numerical approximation of zero. Inset shows the derivative of the steady-state profile $\bar{h}'(x)$, which is of the same shape with the eigenfunction.

limit). In this "intermediate fill ratio" regime, the widths of the core and the tail are comparable, i.e., $L_1\sim L_3$, and they have a similar "degree of flatness." Therefore, this limit is more appropriate for obtaining the pseudo-steady-state profile of an intermediate fill ratio.

## IV. COARSENING MECHANISMS

Based on the knowledge of the pseudo-steady-state profiles in the previous section, we implemented both theoretical and numerical analyses of the coarsening in one dimension to gain insight into the two-dimensional experiments. We will identify, through the linear stability analysis of the steady-state profiles, two coarsening mechanisms responsible for the phenomena observed.

We first examine the linear stability of the steady states derived in Sec. III by adding disturbances as

$$h(x,t)=\bar{h}(x)+\delta\psi(x)e^{\omega t}, \tag{30}$$

where $\delta$ is a small parameter. The perturbation $\psi(x)$ is periodic in $x$ and has zero mean, i.e., $\int\psi(x)dx=0$ for mass conservation. Substituting Eq. (30) into Eq. (1) and retaining only the linear terms yields

$$\omega\psi=\frac{d}{dx}\left\{\bar{h}^3\frac{d}{dx}\left[r(x)\psi-\frac{d^2\psi}{dx^2}\right]\right\}=\mathcal{L}\psi, \tag{31}$$

where $r(x)=\frac{dg(\bar{h})}{dx}=\frac{dg(\bar{h})}{d\bar{h}}\frac{d\bar{h}}{dx}$.

The pseudosteady state is linearly unstable if at least one eigenvalue for the linear operator $\mathcal{L}$ has a positive real part. Since $\mathcal{L}$ in Eq. (31) is singular, we reformulate the linearized equation by introducing a symmetric linear operator $\mathcal{I}$,

$$\mathcal{I}\phi=\frac{d^4\phi}{dx^4}+\frac{d}{dx}\left[r(x)\frac{d\phi}{dx}\right], \tag{32}$$

that can be solved numerically with better accuracy. Others have shown that [19] the eigenvalue problem $-\bar{h}^3\mathcal{I}\phi=\omega\phi$ has the same set of eigenvalues $\omega$ as the original eigenvalue problem $\mathcal{L}\psi=\omega\psi$ with eigenfunctions related to by $\psi=d\phi/dx$.

We discretize $\bar{h}(x)$ and solve $-\bar{h}^3\mathcal{I}\phi=\omega\phi$ numerically for the eigenvalues and the corresponding eigenfunctions. In the following, we examine the stability of the pseudo-steady-state profiles with different periods $\lambda$ but the same fill ratio (e.g., $h_0=0.7$). The smallest computational domain of interest is $L=\lambda_{\max}$ with only one pillar present, as shown in Fig. 8(a), since $\lambda_{\max}$ is the fastest growing wavelength obtained from the linear stability analysis for a flat film $h=h_0$. Computations produce only one positive eigenvalue, $\omega_1=4.19\times10^{-4}$, and the corresponding eigenfunction is shown in Fig. 8(b). Comparing the unstable eigenfunction with the pseudo-steady-state profile reveals this to be a translation mode, which simply shifts the steady-state profile in $x$ direction. In fact, since the steady state is periodic, a zero eigenvalue always exists for Eq. (31) with a corresponding eigenfunction equal to the derivative of the height profile, $\psi=\bar{h}'(x)$. Clearly, the eigenfunction shown in Fig. 8(b) coincides with $\bar{h}'(x)$ in the inset. Therefore, $\omega_1=4.19\times10^{-4}$ is a "numerical approximation" of zero and the steady-state profile with only one period in the domain is stable. In our latter studies, we will simply ignore the eigenvalue associated with the translational mode.

Next, we study the stability of the same steady-state profile but with two periods, i.e., $L=2\lambda_{\max}$, and obtain two positive eigenvalues $\omega_1=0.08$ and $\omega_2=4.1\times10^{-4}$ with the corresponding eigenfunctions $\psi_1$ and $\psi_2$ are plotted in Fig. 9. The two unstable modes are qualitatively different. The positive interior and negative boundaries in the first unstable mode $\psi_1$ promote the movement of two pillars toward each other. The effect is clear if we superimpose $\psi_1$ on the steady-state profile. Hence, this unstable perturbation will lead to coarsening event via collision between neighboring pillars. The second unstable perturbation $\psi_2$ is antisymmetric. Superimposing it with the pseudosteady state causes the right pillar to expand at the expense of shrinkage in the left pillar. This is essentially an "Ostwald ripening" phenomenon. Therefore, based on the linear stability analysis of the steady-state profiles,

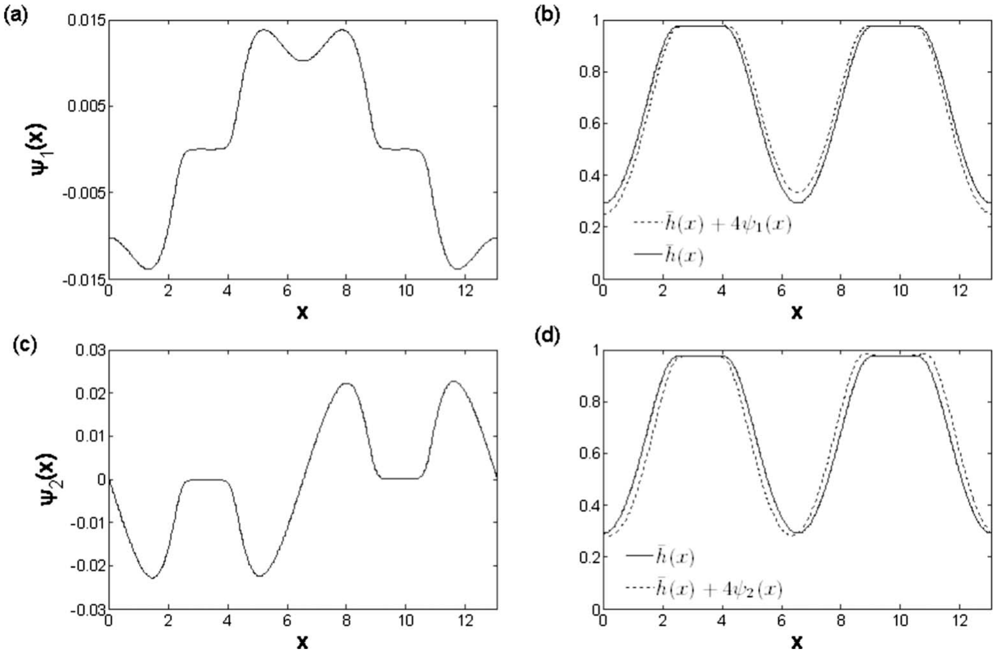

FIG. 9. Two unstable modes for the steady-state profile $\bar{h}(x)$ of fill ratio $h_0=0.7$. (a) The eigenfunction $\psi_1(x)$ with its corresponding eigenvalue $\omega_1=0.08$ and (b) its superimposition with $\bar{h}(x)$. (c) The eigenfunction $\psi_2(x)$ with its corresponding eigenvalue $\omega_2=4.1\times10^{-4}$ and (d) its superimposition with $\bar{h}(x)$. The factor 4 is chosen to magnify the effect of perturbation so that it can be recognized easily in the figure.

two types of coarsening mechanisms can be identified: collision and Ostwald ripening. Both modes would result in the coalescence of neighboring pillars. But the first unstable mode dominates at the fill ratio $h_0=0.7$ since the corresponding eigenvalue $\omega_1=0.08$ is much larger than the second one $\omega_2=4.1\times10^{-4}$. For lower fill ratios, those two types of unstable perturbations persist, but the eigenvalue for Ostwald ripening becomes larger than for the collision mode.

We also calculated the eigenvalues of $\bar{h}(x)$ with $\lambda=\lambda_{\max}$ but with different domain sizes $L=n\lambda_{\max}$. Table I lists ten largest eigenvalues for $n=1$ to 4. "Truly" positive eigenvalues always exist if $L>\lambda_{\max}$. Therefore, the steady-state profile is linearly stable within a domain allowing for only one period and linearly unstable when the domain contains two or more periods. This is consistent with the analytical analysis of a generalized type of Cahn-Hilliard equation [19]. The largest eigenvalue for $L=4\lambda_{\max}$ is the same with the one obtained for $L=2\lambda_{\max}$ and the corresponding eigenfunction has a similar shape in Fig. 9, but with two periods. Thus, the most unstable mode has a period twice that of the pseudo-steady-state profile, as has been observed in spinodal decompositions [21]. But in our system, the "collision" mode is dominant especially for high fill ratios, while the "collapse" mode is the most unstable mode in spinodal decomposition for low concentration of droplets [21].

TABLE I. Ten largest eigenvalues for the steady state $\bar{h}(x)$ ($h_0=0.7$) with a period of $\lambda_{\max}$ in different domain sizes $L$. The data highlighted in gray are (numerical) positive eigenvalues and the bold ones are numerical approximations of "zero" eigenvalues (identified by inspecting their corresponding eigenfunctions).

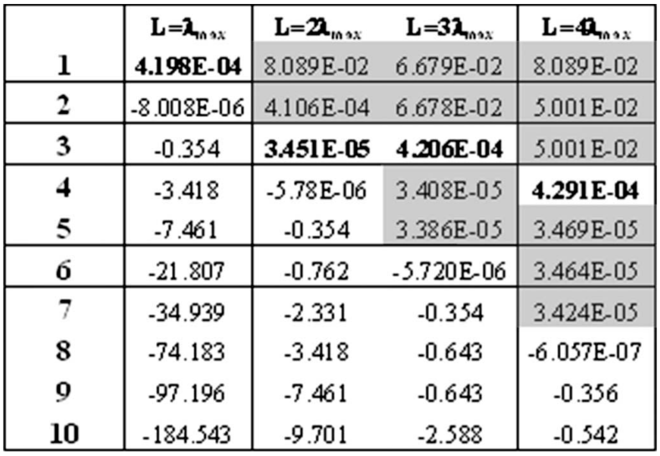

| | $L=\lambda_{max}$ | $L=2\lambda_{max}$ | $L=3\lambda_{max}$ | $L=4\lambda_{max}$ |
|---|---|---|---|---|
| **1** | **4.198E-04** | 8.089E-02 | 6.679E-02 | 8.089E-02 |
| **2** | -8.008E-06 | 4.106E-04 | 6.678E-02 | 5.001E-02 |
| **3** | -0.354 | **3.451E-05** | **4.206E-04** | 5.001E-02 |
| **4** | -3.418 | -5.78E-06 | 3.408E-05 | **4.291E-04** |
| **5** | -7.461 | -0.354 | 3.386E-05 | 3.469E-05 |
| **6** | -21.807 | -0.762 | -5.720E-06 | 3.464E-05 |
| **7** | -34.939 | -2.331 | -0.354 | 3.424E-05 |
| **8** | -74.183 | -3.418 | -0.643 | -6.057E-07 |
| **9** | -97.196 | -7.461 | -0.643 | -0.356 |
| **10** | -184.543 | -9.701 | -2.588 | -0.542 |

We can also identify these two coarsening mechanisms from the experimental images. For example, in Fig. 10(a), pillars 1, 2, and 3 are well separated initially. The movement of pillar 2 toward pillars 1 and 3 is evident between 1230s and 2140s, finally resulting in a coarsening by collision of three pillars. The majority of coarsening observed was through collisions for both thin and thick films. Coarsening by Ostwald ripening is shown in Fig. 10(b). Those tiny pillars indicated by red arrows shrink and eventually disappear entirely. The pillar pointed out by the pink arrow also shrinks significantly, accompanied with the growth of its neighboring pillar. But the highlighted pillar is still present after almost 30 000 s. Overall Ostwald ripening was not observed as extensively as collisions and occurred mainly in relatively thin films.

In addition, a third kind of coarsening mechanism is identified in Fig. 10(c), i.e., collision-induced collisions. After two pillars merge into a larger noncircular one, relaxation toward a circular periphery leads to the engulfment of neigh-

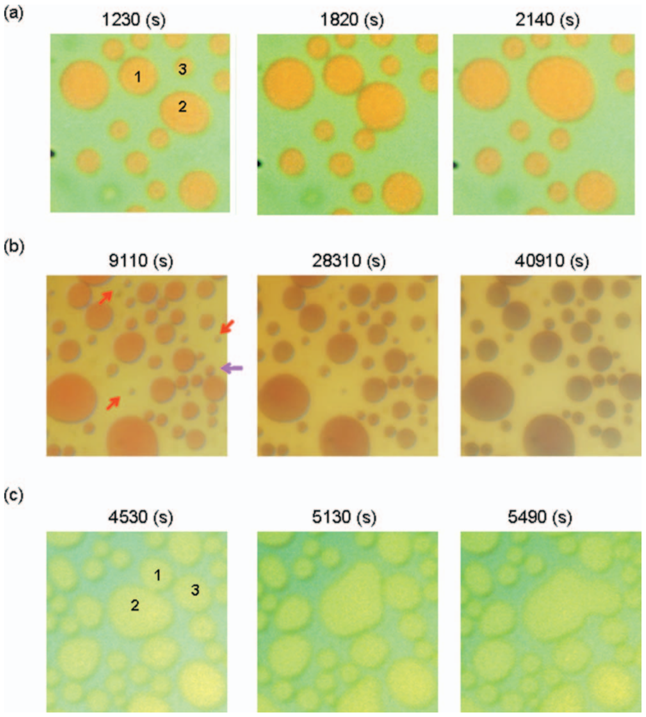

FIG. 10. (Color) Optical images showing three different kinds of coarsening mechanisms: (a) collision (100-nm-PDMS film with a viscosity of 100*k* cSt; (b) Ostwald ripening (100-nm-PDMS film with 10*k* cSt viscosity); (c) collision-induced collisions (160-nm-PDMS film with 600*k* cSt viscosity).

boring pillars that are close enough. Therefore, a pillar experiencing one collision could have a higher probability for a subsequent collision, especially, in a close-packed regime.

## V. SCALING LAW

After identifying different coarsening mechanisms, in the following, we will reduce the original PDE (1) into a pair of ODEs that describes the interaction between pillars and provides a basis for simulating the coarsening process. The method was first outlined by Glasner and Witelski [12,20] in the study of long-time coarsening of dewetting droplets. Since coarsening is a slow process, it is appropriate to select a new time scale $\tau = \delta t$ and $\delta \sim O(h_{\min}^3)$ is a small parameter. The pseudosteady state of each individual pillar is characterized by its center of mass $X(\tau)$ and "pressure" $Q(\tau) = \ln|P(\tau) - P_0|$. We assume that both $X(\tau)$ and $Q(\tau)$ vary slowly with time, so we can approximate the thickness profile as

$$h(x,t) = \bar{h}[x - X(\tau), Q(\tau)] + \delta\psi(x,\tau) + O(\delta^2). \tag{33}$$

Substituting Eq. (33) into Eq. (1) yields

$$-\frac{\partial\bar{h}}{\partial x}\frac{dX}{d\tau} + \frac{\partial\bar{h}}{\partial\bar{Q}}\frac{dQ}{d\tau} = \frac{\partial}{\partial x}\left\{\bar{h}^3\frac{\partial}{\partial x}\left[r(x)\psi - \frac{\partial^2\psi}{\partial x^2}\right]\right\} = \mathcal{L}\psi, \tag{34}$$

with the boundary conditions $J_+ =: -h^3\frac{\partial P}{\partial x}\big|_{x=L/2}$ and $J_- =: -h^3\frac{\partial P}{\partial x}\big|_{x=-L/2}$, assuming the center of the pillar is located at the origin of the domain $-L/2 < x < L/2$. The existence of a solution $\psi$ for the inhomogenous equation (34) is governed by the Fredholm alternative theorem [12], i.e., the solution of $\mathcal{L}\psi = f$ exists if and only if $\langle f, v\rangle = 0$ for all $v$, in which $\mathcal{L}^\dagger v = 0$ and $\mathcal{L}^\dagger$ is the adjoint operator of $\mathcal{L}$. The adjoint of the singular operator $\mathcal{L}$ is

$$\mathcal{L}^\dagger v = \left[r(x) - \frac{\partial^2}{\partial x^2}\right]\left[\frac{\partial}{\partial x}\left(\bar{h}^3\frac{\partial v}{\partial x}\right)\right], \tag{35}$$

and the null space of $\mathcal{L}^\dagger$ is spanned by a pair of eigenfunctions

$$v_1(x) = 1 \quad \text{and} \quad v_2(x) = \int_0^x \frac{\bar{h}(x') - h_{\min}}{\bar{h}(x')^3}dx'. \tag{36}$$

Taking the inner product of the left-hand side of Eq. (34) and $v_i(x)$ provides two governing equations for the time evolution of the $i$th droplet's position and pressure,

$$\frac{dX_i}{dt} = -C_X(Q_i)(J_{i+1,i} + J_{i,i-1}),$$

$$\frac{dQ_i}{dt} = -C_Q(Q_i)(J_{i+1,i} - J_{i,i-1}), \tag{37}$$

where $C_X$ is the drift coefficient

$$C_X(Q_i) = \frac{\int_{-W/2}^{W/2}dx(\bar{h}_i - h_{\min,i})/\bar{h}_i^3}{2\int_{-W/2}^{W/2}dx(\bar{h}_i - h_{\min,i})^2/\bar{h}_i^3} > 0, \tag{38}$$

$C_Q(Q_i)$ is the mass-exchange coefficient

$$C_Q(Q_i) = \left[\int_{-W/2}^{W/2} dx\, \partial\bar{h}_i/\partial Q_i\right]^{-1} = \left[\frac{\partial M_i}{\partial Q_i}\right]^{-1} < 0, \tag{39}$$

and $J_{i+1,i}$ is the flux between the $i$th and $(i+1)$th pillars

$$J_{i+1,i} = -h^3\frac{\partial P}{\partial x} \approx -h_{\min}^3\frac{P_{i+1} - P_i}{(X_{i+1} - W_{i+1}/2) - (X_i + W_i/2)}$$

$$= -h_{\min}^3\frac{\exp(Q_{i+1}) - \exp(Q_i)}{(X_{i+1} - W_{i+1}/2) - (X_i + W_i/2)}. \tag{40}$$

Equations (37) imply that the net sum of the fluxes from both sides of the $i$th pillar determines its lateral motion, while the difference between fluxes controls the extent of the pillar's growth.

With the governing equations for the positions and masses of pillars, we can simulate coarsening among a large numbers of pillars and monitor the time evolution of them by integrating Eqs. (37). We construct a one-dimensional array of $N_0$ pillars located in the domain $0 < x < K$ with $K$ is chosen to accommodate $N_0$ pillars with average spacing $\lambda$. The mass and position of each pillar are random numbers from normal distributions with mean of mass $\bar{M} = h_0K/N_0$ and period $\bar{\lambda} = \lambda$. The standard deviation $\sigma$ can be varied. The $i$th pillar is characterized by its "pressure" $Q_i$, the minimal thickness $h_{\min,i}$, location $X_i$, width $W_i$, and mass $M_i$, as the initial conditions for Eqs. (37). The drift and mass-exchange

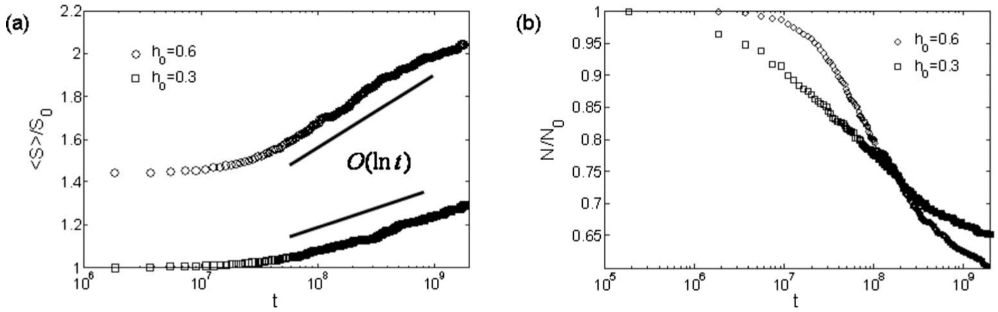

FIG. 11. [(a) and (b)] Simulation results for coarsening at two different fill ratios. The initial pillar sizes follow a normal distribution with the ratio of standard deviation to mean mass being constant: $\sigma/\bar{M}=0.05$. $S_0$ corresponds to the initial (averaged) surface area of one individual pillar and $N_0$ is the initial number of pillars (500).

coefficients can be obtained numerically as a function of pressure, from the pseudo-steady-state profiles that we have obtained in Sec. III B. We then integrate Eqs. (37) numerically to follow $X_i(t)$ and $Q_i(t)$. Coarsening events occur between two pillars due to either of the two mechanisms: collision and Oswald ripening. First, two pillars collide when their tails overlap such that

$$|(X_{i+1} - W_{i+1}/2) - (X_i + W_i/2)| \leq \delta. \qquad (41)$$

At this point, the denominator in Eqs. (40) becomes very small and the local flux is very large so pillars $i$ and $i+1$ start to merge. Since the time for merging is much shorter than the time scale of coarsening, we consider it to happen instantaneously. Once Eq. (41) is satisfied, we eliminate the two "old" pillars and create a new one with mass the sum of the two merging ones and location at the center of mass of both pillars. Integration of the ODE system restarts for the remaining $N-1$ pillars. The second mechanism for coarsening is the collapse of one pillar, i.e., when its mass is reduced to a critical value, its mass is absorbed quickly by the neighbors. We then eliminate that pillar and transfer all the mass to the neighbors as a coarsening event.

Figures 11(a) and 11(b) show the simulation results for coarsening at two different fill ratios $h_0=0.3$ and $h_0=0.6$. In both cases, the initial number of pillars is $N_0=500$ and the initial pillar sizes follow a normal distribution with mean mass $\bar{M}=h_0K/N_0$. The standard deviation to mean mass $\sigma/\bar{M}$ is 0.05 for both cases. For $h_0=0.3$, the average spacing between pillars $\bar{\lambda}$ is equal to $\lambda_{\max}$ at time zero. For the high fill ratio $h_0=0.6$, $\bar{\lambda}$ is set equal to $1.44\lambda_{\max}$ initially because $h_{\min}$ is too large for $\lambda=\lambda_{\max}$, violating our assumption that $h_{\min}$ is small. Clearly, both the average pillar area and the number of pillars follow with straight lines that scale with logarithm of time, in consistency with our experimental observations. Moreover, the coarsening rate is slower for smaller fill ratio, which captures another key feature in our experimental results. Similar effect has also been observed in fully nonlinear numerical simulations [5,22]. The ratio of coarsening due to collision and Ostwald ripening are also quite different for low and high fill ratios. Collision is the main cause at coarsening for high fill ratios, while Ostwald ripening is dominant at low fill ratios.

Interestingly, the coarsening rate also depends on the initial distribution of pillar sizes. As illustrated in Figs. 12(a) and 12(b), coarsening starts later if the initial standard deviation in pillar size is smaller. This is understandable because the "polydispersity" in initial masses also relates to the polydispersity in pressures. Since both motion and growth of pillars depend on pressure differences, a narrower size distribution will make coarsening more difficult to start. We analyzed our experimental results for the size and circularity distributions of individual pillars at the early stage of coarsening for two different fill ratios, as shown in Figs. 12(c)–12(f). Clearly, lower fill ratio tends to engender more uniform pillar arrays and the array has more population of cylindrical shapes than in high fill ratio. Therefore, the lower coarsening rate at low fill ratios can be attributed to at least two aspects: (1) the distance between pillars is longer and (2) the array of pillars is more uniform in sizes and shapes. Ideally, a "monodisperse" array of pillars would take an infinitely long time to coarsen. However, once coarsening starts, the system with lower polydispersity coarsens faster (though still following a logarithm scaling), while more "polydisperse" arrays tend to coarsen gradually. This could provide useful insight for controlling both the onset and rate of coarsening in experiments.

It is interesting to note that the logarithmic coarsening in the electrohydrodynamic patterning is different from spinodal dewetting of thin liquid films on substrates, where power laws were observed experimentally [11] and predicted theoretically [12,23]. In most of the spinodal dewetting studies, an individual droplet sitting on substrate is unbounded from top and its pressure can be easily changed by changing the curvature at the top surface of the droplet. So the driving force, i.e., the pressure difference between neighboring droplets can be large if they differ a lot on the top surface curvatures. Logarithmic scaling was predicted, however, for dewetting of large droplets, where gravity makes the top surfaces flat and mesalike [18]. The "confinement" of droplet's top surface by gravity makes pressure difference between neighboring droplets much smaller, hence, slowing down the coarsening process. In the current study, the polymeric pillars are also bounded by both top and bottom electrodes and the confinement effect of disjoining pressures near both electrodes has the similar effect of gravity to the large

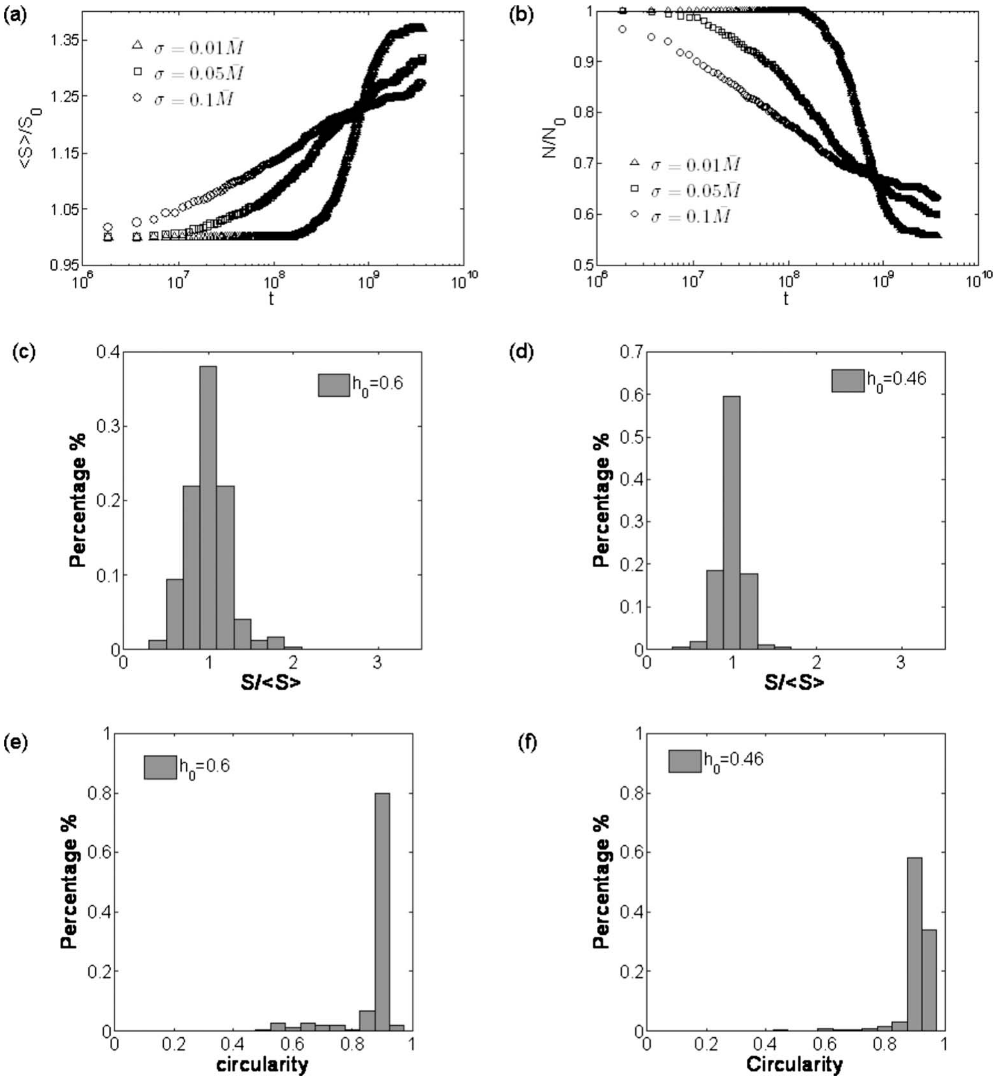

FIG. 12. [(a) and (b)] Coarsening at the same fill ratio ($h_0=0.3$) but with different initial "polydispersity," i.e., $\sigma=0.01\bar{M}$, $0.05\bar{M}$, and $0.1\bar{M}$. [(c)–(f)] Analyses of experimental results at the initial stage (array of pillars) of coarsening of PDMS films (100*k* cSt) at different fill ratios. [(c) and (d)] Histograms of the individual pillar area. [(e) and (f)] Histograms of the circularity of individual pillars, where circularity is defined as $C=4\pi\times\text{area}/\text{perimeter}^2$.

dewetting droplets. Therefore, the coarsening kinetics is similar for both cases but different from unbounded spinodal dewetting. At early stages, spinodal dewetting typically produces arrays of droplets with much larger size variations than electrohydrodynamic patterning, the high polydispersity in terms of droplet size could be another reason why coarsening in spinodal dewetting tends to be faster.

Although our one-dimensional theory captures essential aspects of experiments, 2D structures, the extension of the current study to two-dimensional models will shed lights on other intriguing questions related to coarsening. For example, for fill ratios that are high enough, coarsening of pillars will finally lead to a continuous matrix with circular holes [15,22], which corresponds to the thermodynamically stable state [5]. This phase inversion driven by coarsening can only be studied in 2D models. Since the geometric confinement of disjoining pressure has significant effects on coarsening kinetics, it will be interesting to extend the current study to confined spinodal dewetting [24] and compare the coarsening kinetics with unbounded cases.

## VI. SUMMARY

We have examined the long-time behavior of the EHD instability at the interface between two insulating fluids. This study is motivated by both experimental and numerical evidences that the periodic structures formed at early stages are not stable but tend to merge with each other at later stages. Our microscopic observations clearly show three distinct stages of the coarsening dynamics. In the first stage, the average pillar size increases slowly due to occasional merging between neighboring pillars, while the overall pattern remains almost unchanged. Most coarsening takes place during the second stage characterized by a logarithmic relationship between the average pillar size and time. In the final stage, coalescence becomes much slower presumably because the ultra thin residual layer between pillars renders further merging very slow. The effect of fill ratio or initial film thickness on the coarsening dynamics is also significant.

To understand the coarsening phenomenon, we first identify the solutions of thermodynamically stable and pseudosteady states. We then employ perturbative methods to study the stability of the pseudosteady states, which reveals two different coarsening mechanisms: collisions between pillars and Ostwald ripening. These can also be identified from the experiments. We then reduced the original PDE into a pair of ODEs that govern the interaction between pillars through the two coarsening mechanisms. From simulations governed by these evolution equations, a logarithm scaling law is obtained for both low and high fill ratios with a slower coarsening rate for lower fill ratios. Both are consistent with experimental observations. We have also found that the coarsening depends on the initial size distribution of the pillar array. More uniform arrays tend to start coarsening later but then coarsen faster than more "disperse" arrays. This finding could be utilized in experiments for controlling the onset and speed of coarsening.

This coarsening phenomenon, in morphology, resembles coarsening in spinodal decomposition of a binary mixture and dewetting of thin liquid films. The mechanism, however, differs qualitatively due to the significant effect of Maxwell stresses and geometric confinement on the disjoining pressure at both top and bottom electrodes, which leads to the logarithm scaling law, as we have found both experimentally and numerically.

## ACKNOWLEDGMENTS

This work was funded by NSF MRSEC Program (Grant No. NSF-DMR-0213706).

---

[1] Y. N. Xia and G. M. Whitesides, Annu. Rev. Mater. Sci. **28**, 153 (1998).

[2] S. Y. Chou and L. Zhuang, J. Vac. Sci. Technol. B **17**, 3197 (1999).

[3] E. Schäffer, T. Thurn-Albrecht, T. P. Russell, and U. Steiner, Nature (London) **403**, 874 (2000).

[4] L. F. Pease and W. B. Russel, Langmuir **20**, 795 (2004).

[5] N. Wu and W. B. Russel, Ind. Eng. Chem. Res. **45**, 5455 (2006).

[6] N. Wu, L. F. Pease, and W. B. Russel, Adv. Funct. Mater. **16**, 1992 (2006).

[7] J. S. Langer, Rev. Mod. Phys. **52**, 1 (1980).

[8] A. J. Bray, Philos. Trans. R. Soc. London, Ser. A **361**, 781 (2003).

[9] M. Bestehorn, A. Pototsky, and U. Thiele, Eur. Phys. J. B **33**, 457 (2003).

[10] D. Merkt, A. Pototsky, M. Bestehorn, and U. Thiele, Phys. Fluids **17**, 064104 (2005).

[11] R. Limary and P. F. Green, Phys. Rev. E **66**, 021601 (2002); Langmuir **19**, 2419 (2003).

[12] K. B. Glasner and T. P. Witelski, Phys. Rev. E **67**, 016302 (2003).

[13] A. Sharma and R. Verma, Langmuir **20**, 10337 (2004).

[14] W. S. Rasband, IMAGEJ, U. S. National Institutes of Health, Bethesda, Maryland (http://rsb.info.nih.gov/ij/), 1997–2008.

[15] N. E. Voicu, S. Harkema, and U. Steiner, Adv. Funct. Mater. **16**, 926 (2006).

[16] E. Schäffer, T. Thurn-Albrecht, T. P. Russell, and U. Steiner, Europhys. Lett. **53**, 518 (2001).

[17] A. L. Bertozzi, G. Grun, and T. P. Witelski, Nonlinearity **14**, 1569 (2001).

[18] M. B. Gratton and T. P. Witelski, Phys. Rev. E **77**, 016301 (2008).

[19] R. S. Laugesen and M. C. Pugh, Arch. Ration. Mech. Anal. **154**, 3 (2000).

[20] K. B. Glasner and T. P. Witelski, Physica D **209**, 80 (2005).

[21] J. S. Langer, Ann. Phys. **65**, 53 (1971).

[22] R. Verma, A. Sharma, K. Kargupta, and J. Bhaumik, Langmuir **21**, 3710 (2005).

[23] *Kinetics of Phase Transitions*, edited by S. Puri and V. Wadhawan (CRC, Boca Raton, FL, 2009).

[24] R. Verma, A. Sharma, I. Banerjee, and K. Kargupta, J. Colloid Interface Sci. **296**, 220 (2006).